Journal of Fluids and Structures 115 (2022) 103766

Contents lists available at ScienceDirect

Journal of Fluids and Structures

journal homepage: www.elsevier.com/locate/jfs

A simple mathematical model of retinal reattachment after scleral buckling

Sasan Kheirandish [a,c], Rodolfo Repetto [a], Mario R. Romano [b], Mohammad M. Alishahi [c], Ali A. Golneshan [c], Omid Abouali [c], Jan O. Pralits [a,*]

[a] Department of Civil, Chemical and Environmental Engineering, University of Genoa, Genoa, Italy
[b] Department of Biomedical Sciences, Humanitas University, Milan, Italy
[c] School of Mechanical Engineering, Shiraz University, Shiraz, Iran

ARTICLE INFO

Article history:
Received 1 March 2022
Received in revised form 3 September 2022
Accepted 28 September 2022
Available online xxxx

Keywords:
Rhegmatogenous retinal detachment
Scleral buckling
Fluid–structure interaction

ABSTRACT

Rhegmatogenous retinal detachment (RRD) is a dangerous pathological condition that can lead to blindness and requires surgical treatment. Scleral buckling is a surgical technique that has been in use for many years to repair RRD. It consists in the application of a piece of silicone on the outer surface of the sclera, that pushes the eye wall inwards and modifies its curvature in correspondence of the retinal tear. It is observed that this facilitates retinal reattachment. Various authors speculated that basic principles of fluid mechanics can be invoked to explain the reattachment process, though a convincing explanation of the mechanics underlying the process is still elusive.

In this study, we propose an idealized two-dimensional model of a detached retina, surrounded by liquefied vitreous and study its dynamics secondary to eye movements. This is done using an immersed boundary numerical code. The retinal flaps are modeled as slender one-dimensional elastic bodies, one extremity of which is clamped to the retinal wall. For simplicity we model the retina as a rigid, flat wall. We account for the presence of scleral buckling by inserting a wall bump underneath the detached filaments.

We show that the dynamics of the detached filaments is very complicated and that the presence of a buckle significantly contributes to reduce the time averaged distance between the detached filaments and the wall, thus facilitating reattachment. The mechanisms involved are inherently associated with the dynamics of the filament.

1. Introduction

Rhegmatogenous retinal detachment (RRD) takes place in around 10 out of 100,000 subjects (Mitry et al., 2011) and it is the most common type of retinal detachment (RD). RRD is caused by infiltration of fluid into the subretinal space though a retinal tear, which progressively detaches the neurosensory retina from the retinal pigment epithelium (RPE). Retinal tears are most commonly produced by vitreoretinal tractions, as the result of posterior vitreous detachment (Foulds, 2014). This condition occurs when the vitreous humor contained in the vitreous chamber separates into a gel and a liquid phase. Thus RRD results from a combination of traction on the retina and of intraocular currents in the presence of a retinal hole (Machemer, 1984).

* Corresponding author.
E-mail address: jan.pralits@unige.it (J.O. Pralits).

https://doi.org/10.1016/j.jfluidstructs.2022.103766
0889-9746/

The mechanics of retinal tractions has been quite extensively studied with numerical approaches, in the presence of posterior vitreous detachment (Repetto et al., 2011; Vroon et al., 2018; Di Michele et al., 2020) and vitreous membranes (Repetto et al., 2004). These works highlight the fact that specific regions of the retina, where the adhesion between the vitreous and the retina is strong, are subjected to particularly large mechanical tractions. Such tractions can be produced during eye or head movement (Repetto et al., 2011; Vroon et al., 2018) or can be the result of vitreous gel degradation that leads to a progressive shrinking of the gel phase (Di Michele et al., 2020). The above models justify, from a mechanical perspective, the possible occurrence of retinal breaks. The retinal tearing process induced by a vitreoretinal traction was modeled by Stevens et al. (1992).

Once a retinal break is formed it might or might not evolve into a retinal detachment. Bottega et al. (2013) and Lakawicz et al. (2015) proposed mathematical models of the evolution of a retinal detachment triggered by vitreous contraction that induces extension of vitreous fibrils. Flow of liquefied vitreous induced by movements of the eye is also thought to contribute to retinal detachment, even in the absence of tractions, as it can infiltrate through the retinal break into the subretinal space. This complex phenomenon was studied by Natali et al. (2018) who proposed a simple model of the dynamics of a detached retinal flap. The authors found that the tendency to detach increases with the retinal flap length.

RRD is a serious condition, which needs immediate surgical treatment. The objective of RRD surgery is to induce retinal reattachment and seal retinal tears. Scleral buckling has been in use for several decades and it is still considered one of the most effective procedures to treat RRD (Wang and Snead, 2020). During this surgery a scleral buckle or an encircling band is attached to the outer surface of the sclera, in such a way as to push the sclera inwards, effectively producing a change in curvature of the ocular surface in correspondence of the retinal break. This implies that the RPE is pushed towards the detached flaps, thus reducing the amount of subretinal fluid and facilitating reattachment. Subretinal fluid drainage can also be performed so that, by creating hypotony, the surgeon can induce a more effective scleral wall indentation and reattachment of the retina. Without drainage, the scleral buckle approximates the detached retinal flaps to the RPE but often does not entirely close the retinal break. The retina thus remains detached at the end of surgery and detachment can persist for some time after the surgery. Various mechanical models of the eye bulb deformation produced by scleral buckling have been proposed that help predicting scleral indentation as a function of the geometrical and mechanical properties of encircling bands (Keeling et al., 2009; Ge et al., 2017) or segmental silicon sponges (Wang et al., 2007).

If the RPE is intact it actively pumps water towards the choroid, generating a volume flux per unit retinal surface of approximately 10^{-8} m/s (Dvoriashyna et al., 2018, 2020) This pumping action facilitates reattachment if, after surgery, the retinal tear has been effectively sealed. However, water velocities generated by the RPE pumping are far to low to significantly help the reattachment of a retinal flap if the tear is not closed and water can flow through it during eye rotations.

Reattachment often occurs in the presence of a scleral buckle, even if the retinal tear is not sealed. The mechanisms underlying this finding are still elusive and have been the subject to many speculations. Saccadic eye movements produce flow currents in the liquefied vitreous that have been extensively studied theoretically (e.g. David et al., 1998; Repetto, 2006; Repetto et al., 2010; Silva et al., 2020) and experimentally (e.g. Bonfiglio et al., 2013, 2015). It has been hypothesized that such currents might play a significant role in the reattachment of the retina. A striking evidence supporting this theory comes from very simple experiments performed by Clemens et al. (1987). The experimental setup consisted in a tank containing a free surface liquid (water). The tank could be moved back and forth horizontally, thus generating fluid motion within it. On the bottom of the tank the authors glued a thin transparent membrane (modeling the retina) and they produced a hole into it (a retinal break). Underneath the hole they placed a two-dimensional bump that simulated the presence of a scleral buckle. Fluid was pumped through the hole into the space between the transparent film and the solid wall prior to the start of the experiment, to simulate the condition of a retinal detachment. Interestingly, the authors found that fluid motion in the tank produced a progressive reduction of the 'subretinal' fluid, until the membrane reattached to the wall. When the membrane was not positioned over the wall bump, fluid movement induced no reattachment. Since the membrane was buoyant, the reattachment procedure was entirely produced by hydrodynamic effects induced by the presence of the 'buckle'. Clemens et al. (1987) also proposed a simple two-dimensional, steady, irrotational flow model of their experiments, treating the detached retina as rigid. A somehow similar model has been developed by Foster et al. (2010).

Wong et al. (2018) proposed an interpretation of Clemens et al.'s experiments, based on Bernoulli's principle. In simple terms, they argued that the presence of the bump induces an increase of fluid velocity close to its crest, which, based on Bernoulli's principle, leads to a decrease in pressure in the region of the hole. This, in turn, drives fluid out of the subretinal space, thus effectively facilitating reattachment.

Though sensible and attractive this simple explanation is somehow simplistic as it disregards the dynamics of the flaps that are likely to be extremely complicated and that affect the pressure in the subretinal space. Aim of this work is to propose an idealized model that accounts for this effect and can complement previous contributions in shedding light on the physics behind the effectiveness of the scleral buckling procedure.

2. Formulation of the mathematical model and mechanical properties

2.1. General description of the model

The fluid–structure interaction problem that governs the dynamics of a detached retinal flap in the moving eye is extremely complex. With the aim of capturing the essential mechanical processes involved, while keeping the

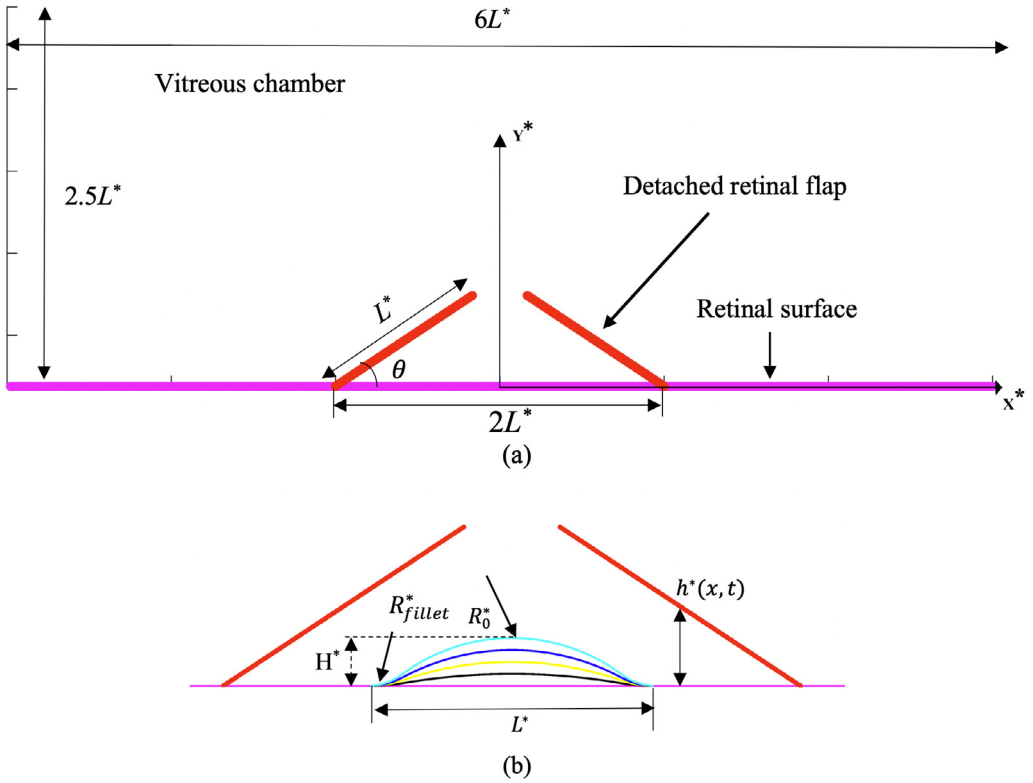

Fig. 1. The study cases including retina filaments and (b) scleral buckling. (a) No scleral buckling case including domain boundary. (b) Scleral buckles with different maximum height values H^* ($H^* = L^*/6$ cyan, $H^* = L^*/8$ blue, $H^* = L^*/12$ yellow, $H^*/24$ black). (For interpretation of the references to color in this figure legend, the reader is referred to the web version of this article.)

problem as simple as possible, we follow the approach proposed by Natali et al. (2018) and consider a two-dimensional approximation. The geometries considered are depicted in Fig. 1.

The eye wall is modeled as a flat, rigid wall (pink in the figure), which moves within its plane in the x-direction. Within our two-dimensional context, a retinal hole is described by a cross-section, consisting of two retinal flaps, each being a slender, massive, inextensible, elastic structure with a given bending stiffness. The three-dimensionality of the hole configuration is modeled by connecting the tips of the two flaps by a virtual linear elastic spring that exerts a force when stretched but not when compressed. Its effect is thus to keep the maximum distance between the tips of the two flaps close to its initial value, while the flaps are free to get closer to each other. The value of the spring constant is set large enough to assure that the maximum distance between the retinal tips remains that of the initial diameter, with an error of less than 1%. Geometrical and mechanical properties of the retinal flap are presented in Table 1.

We assume that the region above the eye wall (the 'interior' of the eye) is occupied by liquefied vitreous and extends to infinity in the y-direction. The assumptions of semi infinite domain and flat wall imply that we neglect the curvature of the eye wall, an assumption which is strictly valid only if the length of the retinal flaps is small compared to the radius of the eye. We note that this assumption has been adopted by many authors who modeled fluid motion in the vitreous chamber in the presence of a retinal break (Foster et al., 2010; Natali et al., 2018).

The liquefied vitreous is modeled as a purely viscous fluid with the same mechanical properties as water and fluid flow is generated by motion of the retinal surface. We consider a harmonic wall motion, thinking of it as of a sequence of saccadic eye rotations of amplitude α and duration d^* in opposite directions, similarly to what was done by Bonfiglio et al. (2015). This implies that the period of oscillations is $D^* = 2d^*$. The amplitude A^* of the wall periodic oscillations is assumed to be $A^* = \alpha R^*/2$, with R^* being the radius of the eye (taken equal to 0.012 m) and the frequency is $\omega^* = 2\pi/D^*$. The corresponding maximum wall velocity is $U^* = \omega^* A^*$. In the lines above and in the following, with superscript stars we indicate dimensional variables.

The presence of a scleral buckle is modeled as a bump located underneath the retinal flaps, with a length L^* and a maximum height H^*, with respect to the undisturbed level of the wall. The bump has the shape of an arc of a circle, with radius R_0^*, smoothly connected to the flat wall with two arcs of radii R^*_{fillet} (see Table 1). The distance between the retinal flaps and the wall is described by the function $h^*(x^*)$, as shown in Fig. 1(b).

Table 1
Parameter values used for the simulations and corresponding references when available.

Quantity	Value	Reference
Properties of the retinal flap		
Density ρ_S^*	1300 kg/m^3	
Length L^*	2.0 mm	
Retinal thickness at the equator h^*	120 μm	Kolb et al. (1995)
Young's modulus E^*	0.24 kN/m^2	Chen et al. (2014)
Bending stiffness $K_b^* = E^* h^{*3}/12$	$3.46 \cdot 10^{-11}$ N m	
Properties of the fluid		
Density ρ_F^*	1000 kg/m^3	Foster et al. (2010)
Dynamic viscosity μ^*	$1.065 \cdot 10^{-3}$ Pa s	Foster et al. (2010)
Scleral parameters		
Height H^*	$L^*/6$, $L^*/8$, $L^*/12$, $L^*/24$	
Radius R_0^*	$0.634L^*$, $0.797L^*$, $1.144L^*$, $2.225L^*$	
Radius R_{fillet}^*	$5/16R_0^*$	
Clamping angle θ	33.56°	

2.2. Governing equations

The governing equations for the fluid and the structure are those found in Natali et al. (2018) and are only briefly described here. We model the detached retina as a one-dimensional inextensible elastic filament of length L^*, with density ρ_S^* and bending rigidity K_b^*, exposed to a viscous incompressible fluid of density ρ_F^* and viscosity μ^*, which is set into motion by a periodic movement of the wall with maximum velocity U^*. The governing equations for the fluid, here given in dimensionless form, are

$$\frac{\partial \mathbf{u}}{\partial t} + (\mathbf{u}\cdot\nabla)\mathbf{u} = -\nabla p + \frac{1}{Re}\nabla^2\mathbf{u} + \mathbf{f}, \tag{1}$$

$$\nabla\cdot\mathbf{u} = 0, \tag{2}$$

where $\mathbf{f}(\mathbf{x}, t)$ is an appropriate volume forcing used to enforce the no-slip condition on the filament. The velocity field is denoted by $\mathbf{u}(\mathbf{x}, t)$, $p(\mathbf{x}, t)$ is the pressure field and $Re = U^* L^* \rho_F^*/\mu^*$ is the Reynolds number. Dimensionless variables have been defined as follows: $\mathbf{x} = \mathbf{x}^*/L^*$, $t = t^* U^*/L^*$, $\mathbf{u}^* = \mathbf{u}^*/U^*$, $p = p^*/(\rho_F^* U^{*2})$, $\mathbf{f} = \mathbf{f}^*/(\rho_F^* U_\infty^{*2}/L^*)$. Here $\mathbf{x} = (x, y) \in \Omega$ are the Cartesian coordinates, with x and y denoting the streamwise and wall-normal direction, respectively, see Fig. 2. The governing equations for a filament are written in a Lagrangian form in terms of the curvilinear coordinate s, that spans the length of the filament. The equations of motion are

$$\rho_1 \frac{\partial^2 \mathbf{X}}{\partial t^2} = \frac{\partial}{\partial s}\left(T\frac{\partial \mathbf{X}}{\partial s}\right) - \frac{\partial^2}{\partial s^2}\left(\gamma\frac{\partial^2 \mathbf{X}}{\partial s^2}\right) - \mathbf{F}, \tag{3}$$

where $T = T^*/(\rho_1^* U_\infty^{*2})$ is the dimensionless tension force along the filament axis, $\gamma = K_b^*/(\rho_1^* U^{*2} L^{*2})$ is the dimensionless bending stiffness, $\rho_1^* = (\rho_S^* - \rho_F^*)a^*$ is the difference between the filament- and fluid densities, a^* is the filament thickness, and $\mathbf{F} = \mathbf{F}^*/(\rho_1^* U_\infty^{*2}/L^*)$ is the dimensionless Lagrangian forcing exerted on the filament by the surrounding fluid. The inextensibility condition (see Huang et al., 2007) is expressed by $\frac{\partial \mathbf{X}}{\partial s}\cdot\frac{\partial \mathbf{X}}{\partial s} = 1$, and the tension force T is determined by the inextensibility condition. On the right hand side of Eq. (3) the first two terms represent the tensional $\mathbf{F}_s$ and bending terms $\mathbf{F}_b$. The last term represents the Lagrangian forces exerted by the fluid on the structure. The value of $\mathbf{F}$ is evaluated using Goldstein's feedback law (Goldstein et al., 1993) in order to impose the no-slip condition on the retinal filaments. Lagrangian and Eulerian forces are linked through a convolution with a discretized version of Dirac delta function δ (see Peskin, 2002).

2.3. Boundary conditions

Referring to the notation used in Fig. 2, boundary conditions for the fluid are given as follows; periodicity between $\partial\Omega_l$ and $\partial\Omega_r$ and $\{\mathbf{u}\cdot\mathbf{n} = 0, \partial(\mathbf{u}\cdot\boldsymbol{\tau})/\partial n = 0\}$ at $\partial\Omega_{top}$ and $\partial\Omega_{bottom}$ (imposed symmetry), where $\mathbf{n}$ and $\boldsymbol{\tau}$ are respectively the normal and tangential directions to the boundary. Since the computational grid for the flow is staggered, no boundary conditions for the pressure are needed (see Natali et al., 2016). Since the filament is clamped to a moving plate with a given angle θ (see Fig. 2), Eq. (3) needs to be solved with proper boundary conditions, both at the clamped and at the free edge:

$$\mathbf{X}|_{s=0} = \mathbf{X}_p(t), \quad \left.\frac{\partial \mathbf{X}}{\partial s}\right|_{s=0} = (\cos\theta, \sin\theta), \quad \left.\frac{\partial^2 \mathbf{X}}{\partial s^2}\right|_{s=L} = 0, \quad \left.\frac{\partial^3 \mathbf{X}}{\partial s^3}\right|_{s=L} = 0. \tag{4}$$

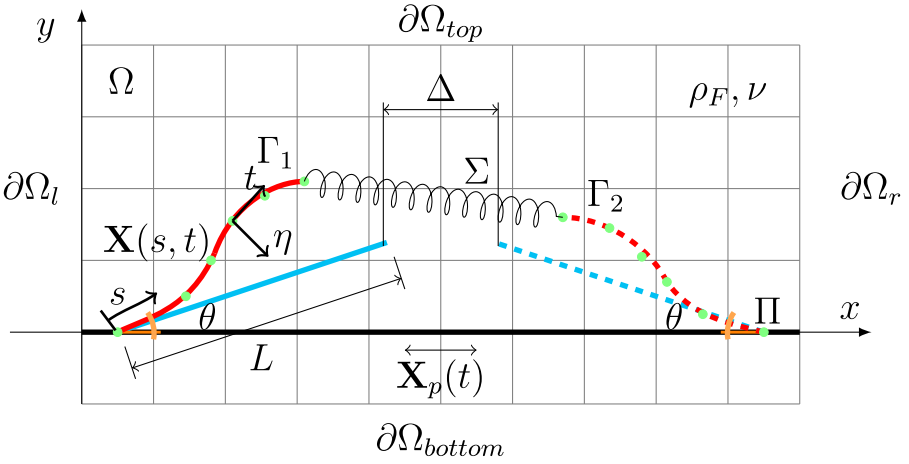

Fig. 2. Schematics of the numerical model. Flaps $\Gamma_{1,2}$ (in red, initial condition in cyan) are clamped at a fixed angle θ to an underlying plate Π that moves with a prescribed motion $\mathbf{X}_p(t)$. The initial distance between the filament tips is indicated with Δ. (For interpretation of the references to color in this figure legend, the reader is referred to the web version of this article.)

The first and second conditions enforce the filament to follow the underlying moving plate and to be clamped with a given angle θ, while the third and fourth conditions state that the bending moment and shear at the free edge is zero, respectively. The free edges are subject to an additional force $\pm k_\Sigma(\mathbf{X}_1 - \mathbf{X}_2)|_{s=L}$ (sign depending on the filament) modeling the tip-connecting spring. The equation for the tension T is solved together with two conditions. The first derives from Eq. (3) and is given as

$$\frac{\partial}{\partial s}\left(T\frac{\partial \mathbf{X}}{\partial s}\right)\bigg|_{s=0} = \mathbf{F} + \mathbf{F}_b + A_P, \tag{5}$$

where A_P is the plate acceleration. The second describes the tension at the filament end $T|_{s=0} = \Sigma(\mathbf{X}_1 - \mathbf{X}_2)$ The solution procedure of the governing equations is identical to the one used in Natali et al. (2018).

2.4. Numerical discretization

The dimensionless computational domain is 6×2.5 in the horizontal and wall-normal directions, respectively. A grid convergence study was conducted comparing 3 different grids, increasing the initial grid by 50% twice. The second grid was chosen for all simulations since the last increment in resolution only resulted in a 2% difference in the temporal and spatial average of the distance between the retinal flap and the wall, see Eq. (7). The chosen grid is uniform in the x-direction, with a grid spacing of 1/60. In the y-direction it is uniform in the region [0, 1.5], with a grid spacing of 1/40, and stretched outside, with a constant stretching ratio of 1.1. The filament is made of 120 uniformly distributed points. In order to reach a trade-off between CFL number for numerical stability ($\sim 10^{-2}$) and no-slip enforcement ($\sim 10^{-2}$), the Goldstein's feedback law coefficients have been set to $\beta_1 = -10$ and $\beta_2 = -100$. Note that these values can be arbitrarily chosen as long as the no-slip condition is satisfied to a pre-defined accuracy. Before running the cases for the current study a few cases from the article by Natali et al. (2018) were reproduced with high accuracy.

3. Results

At the beginning of each simulation the fluid is at rest and the filaments in the their relaxed position. After a transient phase that lasts between 5 and 10 time periods, the solution becomes periodic and the results shown in the following refer to this periodic phase of motion. Note that the non-dimensional time t has been normalized with the corresponding period in this section.

In Figs. 3 and 4 we report various snapshots of the filaments configuration at different times within a cycle of oscillation, for saccades with amplitude $\alpha = 8°$ and 15°, respectively. In the figures we also report flow streamlines and the colors show the pressure distribution. Each column in the figures refers to a given case and time progresses from top to bottom ($t = 0,\ 1/8,\ 1/4,\ 3/8,\ 1/2$). In the leftmost column we show the dynamics of the filaments in the case of a flat retinal surface, i.e. in the absence of a scleral buckle. The second and third columns refer to the cases of scleral indentations with a different maximum height, equal to $H = H^*/L^* = 1/12$ and $H = 1/6$, respectively. The imposed wall movement is such that the wall velocity behaves in time like $\cos(2\pi t)$, therefore the velocity peak is at $t = 0$ (left to right) and at $t = 1/2$ (right to left). Note that, owing to the numerical method adopted, we also solve a fictitious problem underneath

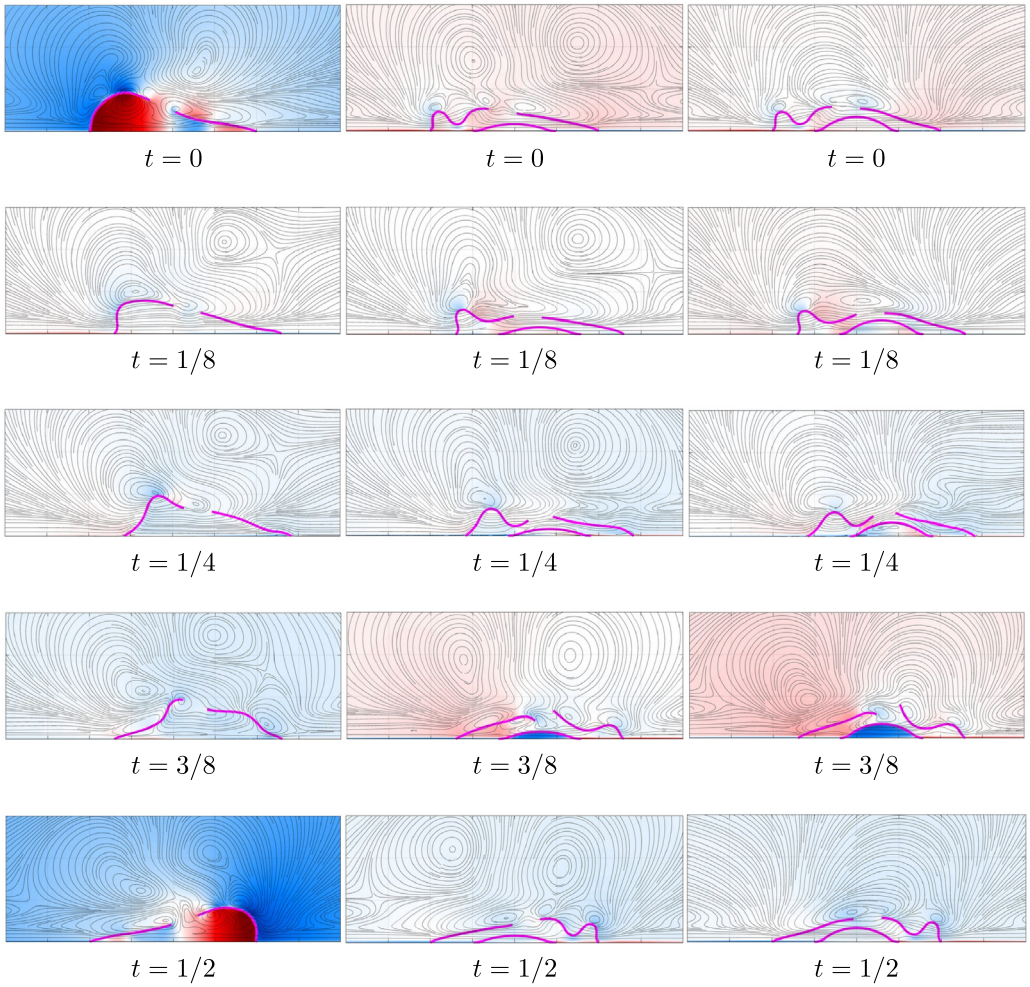

Fig. 3. Filament position, flow streamlines and pressure (color; blue negative, white zero, red positive and the range is [−4:4]) for five time instants in the case of 8° amplitude wall motion (zoomed view area close to retinal filaments). Time progresses from top bottom by columns. Each column refers to a different height of the wall indentation: $H = 0$ (first column), $H = 1/12$ (second column) and $H = 1/6$ (third column). Non-dimensional time t has been normalized by the corresponding period. (For interpretation of the references to color in this figure legend, the reader is referred to the web version of this article.)

the buckle; the solution there, however, has no significance and does not affect the solution in the fluid domain, thus it should be disregarded.

Since the filament is slender and very flexible its dynamics is very complicated, as shown in the figures. At certain time instants the pressure jump across the filament can be relatively large, which is what induces filament motion and also tractions at the attachment points. The dynamics of the filament is significantly modified by the presence of the wall indentation, as clearly shown by the snapshots of Figs. 3 and 4. In particular, the buckling of the filaments is more pronounced in the presence of the wall indentation, especially when the indentation has a large amplitude (right column in the figures). This seems to be a result of the filaments being attracted towards the wall by hydrodynamic effects, and effectively implies that, the filament remains closer to the wall during motion.

To quantify this effect we compute the spatial average of the distance in the y-direction between each filament and the wall, defined as

$$\overline{h}^{(i)}(t) = \frac{1}{N}\sum_{n=1}^{N} h_n^{(i)}(t), \qquad i = \text{left or right}, \tag{6}$$

where N is the number of the discrete material points of filament i. We plot the above quantity, normalized with its undisturbed value $\overline{h}_0^{(i)}$ (the initial value), versus time in Figs. 5 and 6. We note that values of $\overline{h}^{(i)}(t)/\overline{h}_0^{(i)}$ smaller than 1 imply that, at time t, the filament is, on average, closer to the wall than it would be in static conditions.

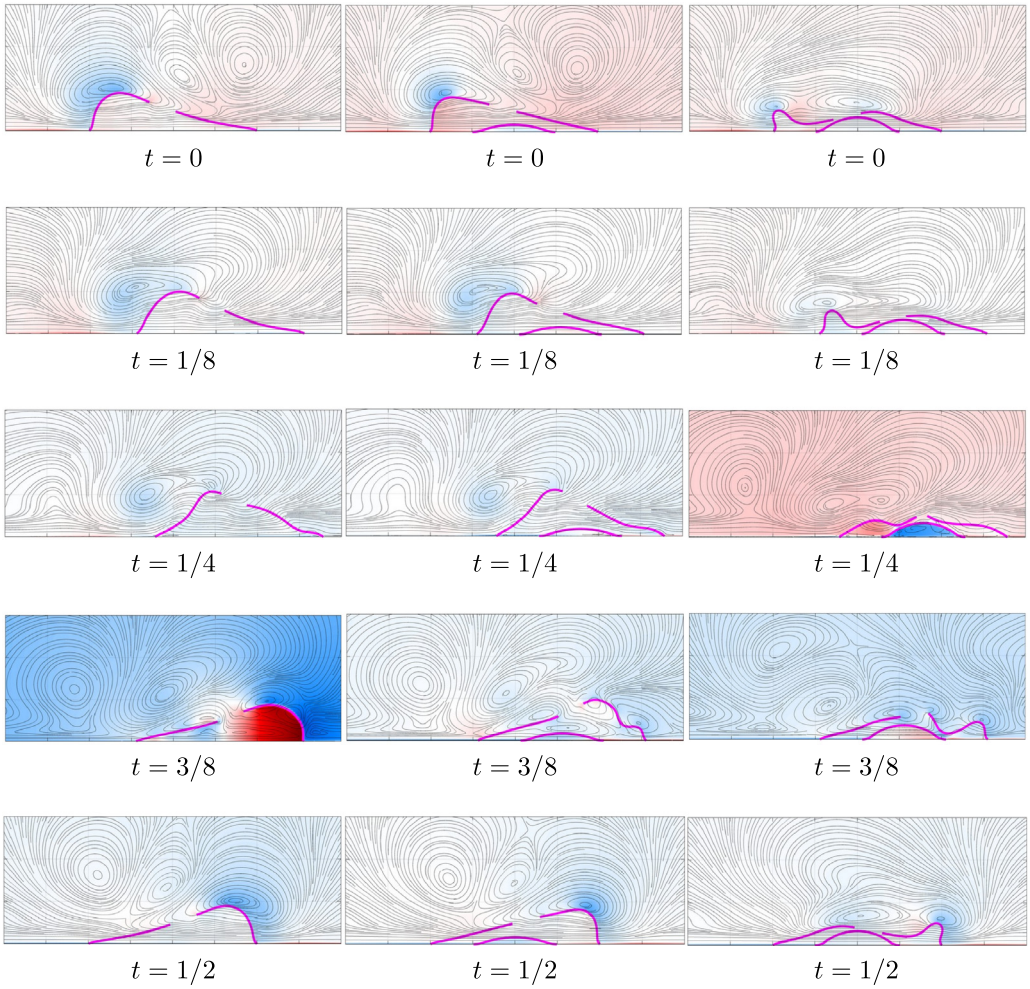

Fig. 4. Filament position, flow streamlines and pressure (color; blue negative, white zero, red positive and the range is [−4:4]) for five time instants in the case of 15° amplitude wall motion (zoomed view area close to retinal filaments). Time progresses from top bottom by columns. Each column refers to a different height of the wall indentation: $H = 0$ (first column), $H = 1/12$ (second column) and $H = 1/6$ (third column). Non-dimensional time t has been normalized by the corresponding period. (For interpretation of the references to color in this figure legend, the reader is referred to the web version of this article.)

Fig. 5(a,b) shows that in the flat wall case (red dashed line) the filament is on average pushed away from the wall when wall velocity is large and attracted towards it otherwise. In all other cases shown in the figure, for wall bumps of maximum different heights from $H = 1/24$ to $H = 1/6$, hydrodynamic effects clearly attract the filaments towards the wall and in all cases and for all times the quantity $\overline{h}^{(i)}/\overline{h}_0^{(i)}$ is smaller than 1.

Interestingly, the situation is slightly different in the case of 15° oscillations, as shown in Fig. 6(a,b). In fact, in this case only sufficiently large wall bumps (large H) are capable of reducing the values of $\overline{h}^{(i)}(t)/\overline{h}_0^{(i)}$, which for small values of H remains close to that corresponding to the flat wall scenario at all times. The difference in distance between the filament and the wall in the cases of $H = 1/12$ and $H = 1/6$ can also be appreciated by comparing the second and third columns of Fig. 4.

Finally, in order to estimate the overall effect of the buckle on the position of the filaments we take a time average of $\overline{h}^{(i)}(t)$ over the oscillation period to obtain

$$\hat{h}^{(i)} = \int_0^1 \overline{h}^{(i)} dt, \qquad i = \text{left or right}. \tag{7}$$

The average distance of the detached retina from the wall is $\hat{h} = 1/2(\hat{h}^{(\text{left})} + \hat{h}^{(\text{right})})$.

In Fig. 7(a,b) we plot the value of $\hat{h}^{(\text{left})}$ (a) and $\hat{h}^{(\text{right})}$ (b) versus the wall indentation maximum height H^*. The blue, green and black curves correspond to three different eye movements, of 8°, 12° and 15°, respectively; the red curve

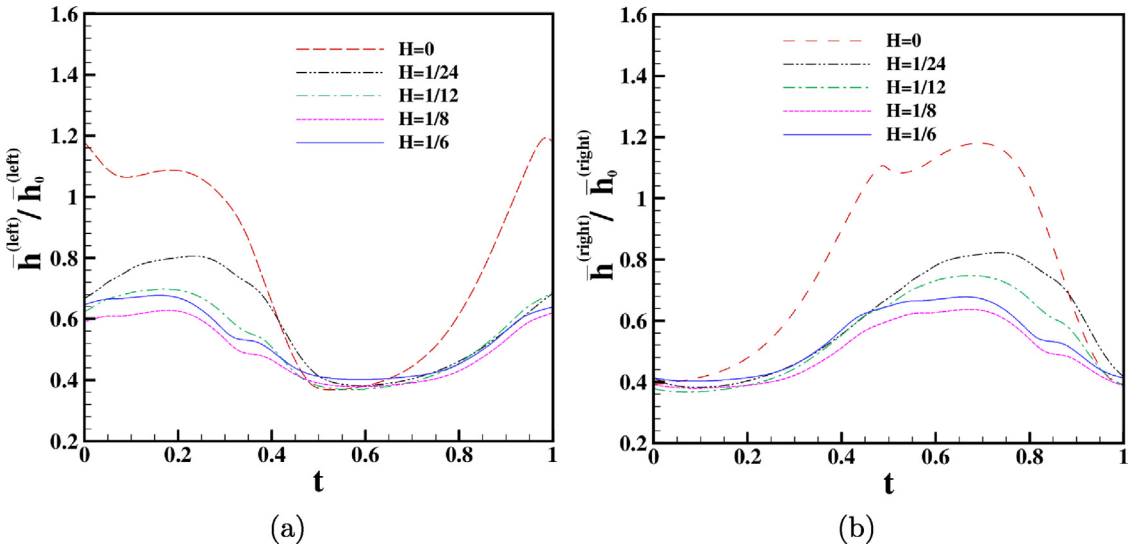

Fig. 5. Normalized space averaged distance between the filament and the wall $\overline{h}^{(i)}/\overline{h}_0^{(i)}$ (i = left or right) plotted versus time. Amplitude of wall motion equal to 8°. (a) left filament, (b) right filament. (For interpretation of the references to color in this figure legend, the reader is referred to the web version of this article.)

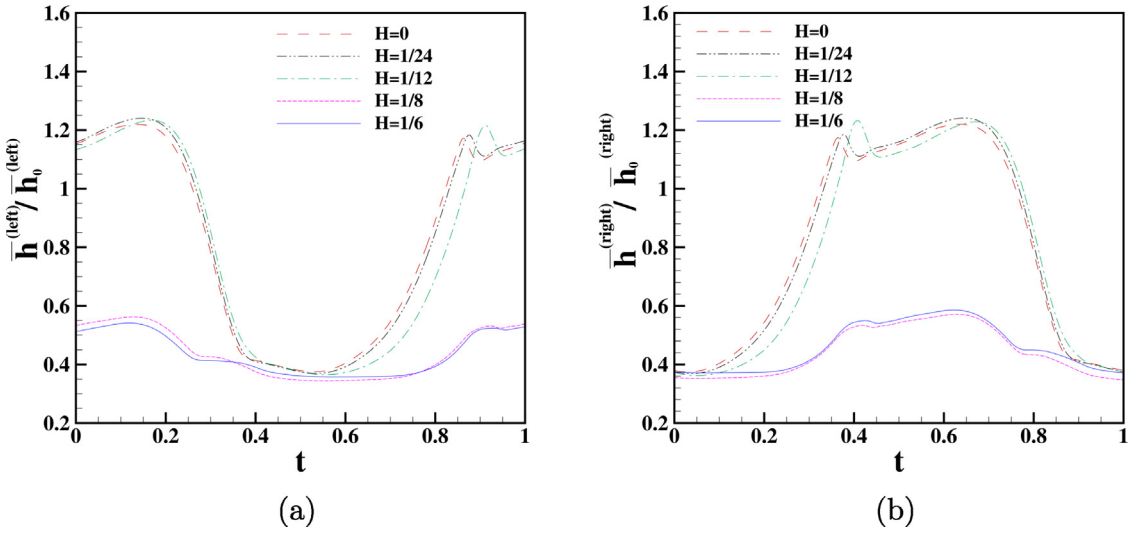

Fig. 6. Normalized space averaged distance between the filament and the wall $\overline{h}^{(i)}/\overline{h}_0^{(i)}$ (i = left or right) plotted versus time. Amplitude of wall motion equal to 15°. (a) left filament, (b) right filament.

is relative to the flat wall case. Since we are considering the case of a periodic motion, left and right filaments have approximately the same dynamics, but with opposite phase. Thus, upon time integration their time and space average distance is approximately the same. This is confirmed by Fig. 7(a,b), where the cases reported in panels (a) and (b) differ by less than 6%. Overall, the figure confirms the results shown earlier: hydrodynamics plays a key role in reducing the average distance between the filaments and the wall. The effect of the wall bump under the filaments is to attract the filaments towards the wall during motion. For small amplitude wall oscillations the average distance between filament and wall reduces smoothly as the height of the bump increases. On the other hand, for wall oscillations of a larger amplitude, the dependency of $\hat{h}^{(i)}$ on H becomes highly nonlinear and the results suggest that only relatively large amplitude wall bumps are effective in reducing the distance of the filament from the wall.

4. Conclusions

In this work we propose a simple numerical model aimed at understanding the fundamental physics behind retinal reattachment in presence of a scleral buckle. The model is based on a simple two-dimensional geometry: we neglect the

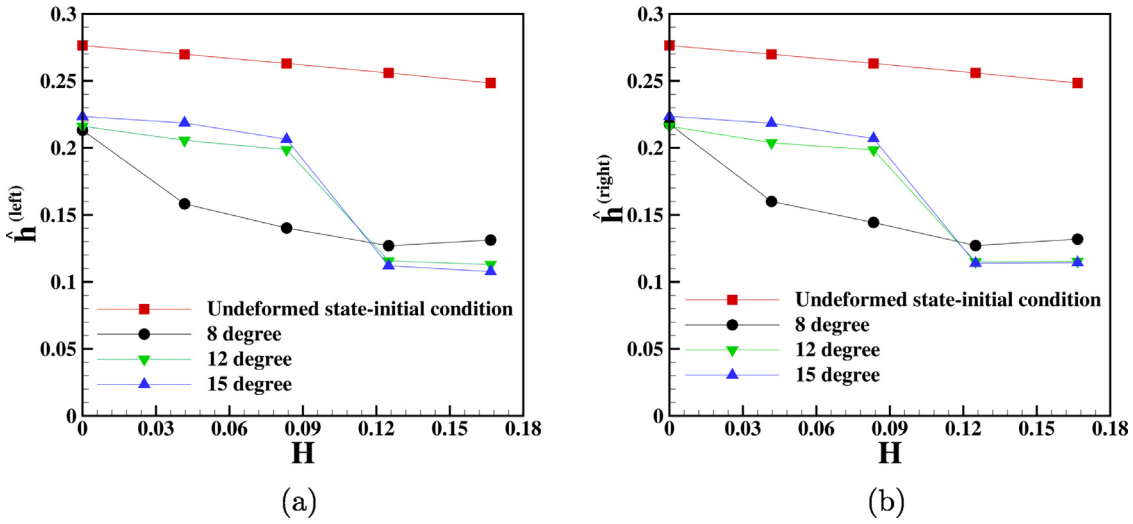

Fig. 7. Integral over time and space average of average distance parameter $\hat{h}^{(i)}$ ($i =$ left or right) plotted versus scleral height, (a) Left filament; (b) Right filament. (For interpretation of the references to color in this figure legend, the reader is referred to the web version of this article.)

curvature of the inner eye wall and model the retinal surface as a flat plate that performs periodic oscillations, which represent saccadic eye rotations. The detached retina is described as a thin elastic membrane, with a given bending stiffness, clamped to the wall. We treat the liquefied vitreous as a viscous, Newtonian fluid. The scleral buckle is modeled as a wall bump, located in correspondence of the retinal break and we study the effect of varying its height. The model is based on assumptions made by various previous authors (e.g. Clemens et al., 1987; Foster et al., 2010; Natali et al., 2018) and we think that the key ingredients to explain why scleral buckling facilitates retinal reattachment are indeed retained. The numerical simulations are based on the use of the immersed boundary method, which is particularly suited for describing the interaction between a moving fluid and a slender solid body. The outputs of the numerical simulations are pressure and velocity fields in the fluid and the dynamics of the filaments. The range of scleral heights used here is large enough to demonstrate its effect on the filament dynamics and reattachment. Heights H larger than 1/6 are not investigated since it was found that the filaments touch the scleral buckle at some point during the periodic motion. Since a model of two solid walls touching is not part of the present mathematical framework such large values of H are avoided.

The work is motivated by the clinical need of understanding the mechanisms behind retinal reattachment after scleral buckling in the absence of fluid drainage, which are not entirely understood. Various authors have, however, attempted to provide physical explanations based on basic fluid mechanics principles (Wong et al., 2018), such as Bernoulli's.

Our work confirms that scleral buckling facilitates retinal reattachment. This is because a wall bump leads to change of the stress acting on the filaments, resulting in a different filament dynamics compared to the flat wall case. The overall result is that, in the presence of a scleral buckle, the average distance between the retinal flap and the wall decreases, thus inducing fluid expulsion from the subretinal space, which facilitates reattachment. The height of the buckle is found to play an important role. In particular, for relatively large wall oscillations amplitudes a decrease of the distance between the moving filament and the wall is achieved only if the wall indentation is large enough.

Though this work confirms the finding of existing simple models, it also shows that the physical interpretation of the role of a scleral buckling proposed by previous authors is somehow simplistic and that the dynamics of the filament itself plays a fundamental role. This is difficult to predict without a model that explicitly accounts for filament motion.

As the model is based on various, quite strong simplifying assumptions, a complete picture of the mechanics of retinal reattachment would require additional modeling work. In particular, future research should consider a more realistic three-dimensional, closed geometry and therefore a three-dimensional implementation of the immersed boundary method. Though this endeavor is certainly possible nowadays, the numerical simulations would be very heavy. In this respect the present work also has the value of showing what are the effects that are likely to matter most and of guiding future more sophisticated numerical works.

CRediT authorship contribution statement

Sasan Kheirandish: Methodology, Software, Validation, Formal analysis, Investigation, Writing – original draft, Writing – review & editing. **Rodolfo Repetto:** Term, Conceptualization, Methodology, Writing – original draft, Writing – review & editing, Supervision. **Mario R. Romano:** Data curation, Writing – original draft. **Mohammad M. Alishahi:** Supervision. **Ali A. Golneshan:** Supervision. **Omid Abouali:** Supervision. **Jan O. Pralits:** Term, Conceptualization, Methodology, Writing – original draft, Writing – review & editing, Supervision, Project administration.

Declaration of competing interest

The authors declare that they have no known competing financial interests or personal relationships that could have appeared to influence the work reported in this paper.

Data availability

Data will be made available on request.

References

Bonfiglio, A., Lagazzo, A., Repetto, R., Stocchino, A., 2015. An experimental model of vitreous motion induced by eye rotations. Eye Vis. 2 (1), 1–10.
Bonfiglio, A., Repetto, R., Siggers, J.H., Stocchino, A., 2013. Investigation of the motion of a viscous fluid in the vitreous cavity induced by eye rotations and implications for drug delivery. Phys. Med. Biol. 58 (6), 1969.
Bottega, W.J., Bishay, P.L., Prenner, J.L., Fine, H.F., 2013. On the mechanics of a detaching retina. Math. Med. Biol.: J. IMA 30 (4), 287–310.
Chen, K., Rowley, A.P., Weiland, J.D., Humayun, M.S., 2014. Elastic properties of human posterior eye: Knowledge of the Mechanical Properties of the Human Eye. J. Biomed. Mater. Res. Part A 102 (6), 2001–2007.
Clemens, S., Kroll, P., Stein, E., Wagner, W., Wriggers, P., 1987. Experimental studies on the disappearance of subretinal fluid after episcleral buckling procedures without drainage. Graefe's Arch. Clin. Exp. Ophthalmol. 225 (1), 16–18.
David, T., Smye, S., Dabbs, T., James, T., 1998. A model for the fluid motion of vitreous humour of the human eye during saccadic movement. Phys. Med. Biol. 43, 1385–1399.
Di Michele, F., Tatone, A., Romano, M.R., Repetto, R., 2020. A mechanical model of posterior vitreous detachment and generation of vitreoretinal tractions. Biomech. Model. Mechanobiol. 19 (6), 2627–2641.
Dvoriashyna, M., Foss, A.J., Gaffney, E.A., Jensen, O.E., Repetto, R., 2018. Osmotic and electroosmotic fluid transport across the retinal pigment epithelium: A mathematical model. J. Theoret. Biol. 456, 233–248.
Dvoriashyna, M., Foss, A.J., Gaffney, E.A., Repetto, R., 2020. Fluid and solute transport across the retinal pigment epithelium: a theoretical model. J. R. Soc. Interface 17 (163), 20190735.
Foster, W.J., Dowla, N., Joshi, S.Y., Nikolaou, M., 2010. The fluid mechanics of scleral buckling surgery for the repair of retinal detachment. Graefe's Arch. Clin. Exp. Ophthalmol. 248 (1), 31–36.
Foulds, W.S., 2014. Role of vitreous in the pathogenesis of retinal detachment. Vitreous Health Dis. 375–393.
Ge, P., Bottega, W.J., Prenner, J.L., Fine, H.F., 2017. On the behavior of an eye encircled by a scleral buckle. J. Math. Biol. 74 (1–2), 313–332.
Goldstein, D., Handler, R., Sirovich, L., 1993. Modeling a no-slip flow boundary with an external force field. J. Comput. Phys. 105, 354–366.
Huang, W.-X., Shin, S.J., Sung, H.J., 2007. Simulation of flexible filaments in a uniform flow by the immersed boundary method. J. Comput. Phys. 226, 2206–2228.
Keeling, S.L., Propst, G., Stadler, G., Wackernagel, W., 2009. A mathematical model for the deformation of the eyeball by an elastic band. Math. Med. Biol.: A J. IMA 26 (2), 165–185.
Kolb, H., Fernandez, E., Nelson, R., 1995. Webvision: the organization of the retina and visual system [internet].
Lakawicz, J.M., Bottega, W.J., Prenner, J.L., Fine, H.F., 2015. An analysis of the mechanical behaviour of a detaching retina. Math. Med. Biol.: A J. IMA 32 (2), 137–161.
Machemer, R., 1984. The importance of fluid absorption, traction, intraocular currents, and chorioretinal scars in the therapy of rhegmatogenous retinal detachments: Xli Edward Jackson memorial lecture. Am. J. Ophthalmol. 98 (6), 681–693.
Mitry, D., Chalmers, J., Anderson, K., Williams, L., Fleck, B.W., Wright, A., Campbell, H., 2011. Temporal trends in retinal detachment incidence in Scotland between 1987 and 2006. Br. J. Ophthalmol. 95 (3), 365–369.
Natali, D., Pralits, J.O., Mazzino, A., Bagheri, S., 2016. Stabilizing effect of porosity on a flapping filament. J. Fluids Struct. 61, 362–375.
Natali, D., Repetto, R., Tweedy, J.H., Williamson, T.H., Pralits, J.O., 2018. A simple mathematical model of rhegmatogenous retinal detachment. J. Fluids Struct. 82, 245–257.
Peskin, C.S., 2002. The immersed boundary method. Acta Numer. 11, 479–517.
Repetto, R., 2006. An analytical model of the dynamics of the liquefied vitreous induced by saccadic eye movements. Meccanica 41, 101–117.
Repetto, R., Ghigo, I., Seminara, G., Ciurlo, C., 2004. A simple hydro-elastic model of the dynamics of a vitreous membrane. J. Fluid Mech. 503, 1–14.
Repetto, R., Siggers, J., Stocchino, A., 2010. Mathematical model of flow in the vitreous humor induced by saccadic eye rotations: effect of geometry. Biomech. Model. Mechanobiol. 9 (1), 65–76.
Repetto, R., Tatone, A., Testa, A., Colangeli, E., 2011. Traction on the retina induced by saccadic eye movements in the presence of posterior vitreous detachment. Biomech. Model. Mechanobiol. 10 (2), 191–202.
Silva, A.F., Pimenta, F., Alves, M.A., Oliveira, M.S., 2020. Flow dynamics of vitreous humour during saccadic eye movements. J. Mech. Behav. Biomed. Mater. 110, 103860.
Stevens, J., Jones, I., Warner, M., Lavin, M., Leaver, P., 1992. Mathematical modelling of retinal tear formation: implications for the use of heavy liquids. Eye 6 (1), 69–74.
Vroon, J., De Jong, J., Aboulatta, A., Eliasy, A., Van Der Helm, F., Van Meurs, J., Wong, D., Elsheikh, A., 2018. Numerical study of the effect of head and eye movement on progression of retinal detachment. Biomech. Model. Mechanobiol. 17 (4), 975–983.
Wang, F., Lee, H.P., Lu, C., 2007. Biomechanical effect of segmental scleral buckling surgery. Curr. Eye Res. 32 (2), 133–142.
Wang, A., Snead, M.P., 2020. Scleral buckling–a brief historical overview and current indications. Graefe's Arch. Clin. Exp. Ophthalmol. 258 (3), 467–478.
Wong, D., Chan, Y.K., Bek, T., Wilson, I., Stefánsson, E., 2018. Intraocular currents, Bernoulli's principle and non-drainage scleral buckling for rhegmatogenous retinal detachment. Eye 32 (2), 213–221.